Electromagnetic global gyrokinetic simulation of shear Alfven wave dynamics in tokamak plasmas

Y. Nishimura and Z. Lin
Department of Physics and Astronomy, University of California, Irvine, California 92697

W. X. Wang
Princeton Plasma Physics Laboratory, Princeton, New Jersey 08543

(Received 10 November 2006; accepted 26 February 2007; published online 12 April 2007)

Electromagnetic gyrokinetic simulation in toroidal geometry is developed based on a fluid-kinetic hybrid electron model. The Alfven wave propagation in a fully global gyrokinetic particle simulation is investigated. In the long-wavelength magnetohydrodynamic limit, shear Alfven wave oscillations, continuum damping, and the appearance of the frequency gap in toroidal geometries are demonstrated. Wave propagation across the magnetic field (kinetic Alfven wave) is examined by comparing the simulation results with the theoretical dispersion relation. Furthermore, finite-beta stabilization of the ion temperature gradient mode and the onset of the kinetic ballooning mode are demonstrated. © *2007 American Institute of Physics*. [DOI: 10.1063/1.2718908]

I. INTRODUCTION

Significant progress in three dimensional gyrokinetic turbulence simulations has been made for electrostatic fluctuations assuming adiabatic electrons.[1] However, in the presence of magnetic perturbations, there exist new branches of modes, for example, toroidicity induced Alfven eigenmodes (TAEs),[2] and Alfvenic ion temperature gradient (AITG) modes[3,4] (or kinetic ballooning modes),[5] that can play important roles in plasma instabilities and transport.

The difficulties of electromagnetic gyrokinetic simulations were the stringent numerical constraints. In gyrokinetic particle-in-cell (PIC) simulations,[6,7] with the electromagnetic perturbations in the system, freely streaming electrons above the local Alfven velocity do not interact with the wave, but do contribute to the accumulation of statistical noise inherent to the PIC method.[8,9] To circumvent these difficulties, a split-weight scheme[10,11] is introduced to treat the adiabatic response of the fast electrons separately from the resonant interaction with the wave by the slow electrons. The split-weight scheme treats the adiabatic response (the freely streaming electrons) analytically, and thus reduces the statistical noise of the particle simulation. Based on similar considerations, a fluid-kinetic hybrid electron model has been proposed.[12] The hybrid model solves for the adiabatic response in the lowest order fluid equations and solves the resonant interaction in the higher order kinetic equations, based on an expansion of the electron response using a small parameter of the square-root of the electron-ion mass ratio, while preserving the linear and the nonlinear wave-particle interactions.

Using the fluid-kinetic hybrid electron model, we can begin to investigate the particle and heat transport due to electromagnetic turbulence in fully global tokamak geometry. The numerical simulation code we employ in this paper is the Gyrokinetic Toroidal Code (GTC).[1] To gain confidence in studying the subtle electromagnetic nonlinear physics, one needs to study the nature of Alfven dynamics step by step, including the origin of the instability drive, the dissipation mechanisms, and the saturation mechanisms in which wave-particle interactions are believed to play an important role. We start by verifying the propagation of shear Alfven waves in the absence of drive or dissipation mechanisms. We verify this both in the magnetohydrodynamic (MHD) limit and in the case with kinetic ions. With the addition of the ion temperature gradient drive, we study the effect of finite-β on the ion temperature gradient mode.

The electron model employed in this paper is the electromagnetic fluid-kinetic hybrid electron model.[12,13] Since it relies on an expansion based on a small parameter, the ratio of the parallel wave phase velocity to the electron thermal velocity, v_{the}, with $\delta_m=(\omega/k_{\|})/v_{\mathrm{the}}$, our hybrid model is not suitable for studying the tearing mode, for which the parallel dynamics near the mode rational surfaces (where $k_{\|}=0$) plays a crucial role.

In the GTC code, we can implement realistic boundary conditions taking advantage of the two dimensional nature of the elliptic field solver (conventionally a Fast Fourier Transform or a one dimensional field solver is employed for local flux-tube-type gyrokinetic simulation codes). As one of the advantages of our global field solver, the GTC code incorporates the effects of spatially varying $k_{\|}$, which allows us to simulate continuum damping and the TAE modes.

In the electrostatic version of the GTC code, an iterative solver in real space[14] has been employed. However, in the presence of nonadiabatic kinetic electrons, the inversion matrix of the gyrokinetic Poisson equation is no longer diagonally dominant,[15] and the iterative solver does not converge. In the simulations presented in this paper, we cast the gyrokinetic Poisson equation into a sparse matrix form, which is inverted by a fast linear solver. The new Poisson solver[16,17] (for global tokamak geometries) with the direct sparse matrix inversion enabled us to study the electron dynamics in the electromagnetic simulation.

The rest of this paper is organized as follows. In Sec. II, we derive the fluid-kinetic electron hybrid model in toroidal

geometry. In Sec. III, we demonstrate Alfven wave propagation in the long wavelength MHD limit. In Sec. IV, as preliminary work to the TAE mode study, the generation of the frequency gap due to toroidal effects is shown. In Sec. V, we study kinetic Alfven waves.[18,19] In Sec. VI, we present a calculation of linear growth rate of the finite-β modified ion temperature gradient (ITG) mode and the excitation of the Alfvenic ITG mode. Section VII summarizes this work.

II. ELECTROMAGNETIC FLUID-KINETIC HYBRID ELECTRON MODEL

We present the electromagnetic fluid-kinetic hybrid electron model in toroidal geometry. The hybrid model in a one-dimensional system was originally proposed by Lin and Chen,[12] and later formulated for toroidal geometry by Wang, Chen, and Lin.[13] We write the equations in cgs-Gaussian units to differentiate ion and electron dynamics and treat waves and instabilities on the ion gyroradius scale.

To begin with, for the equilibrium magnetic field, we take the Clebsch form

$$\mathbf{B}_0 = \nabla\psi_0 \times \nabla\alpha_0,$$

where $\psi_0(r)$ is the poloidal flux label [$\psi_0 = \int B_0(r/q)dr$, where q is the safety factor, r corresponds to the radial coordinate of the polar coordinate system, and B_0 is the magnetic field strength], and $\alpha_0 = q(\psi_0)\theta - \zeta$ is the helical angle. Here, $q(\psi_0)$ is the equilibrium safety factor, and θ and ζ are the poloidal angle and the toroidal angle, respectively. The magnetic field in the presence of the perturbation $\delta\psi(r,\theta,\zeta,t)$ and $\delta\alpha(r,\theta,\zeta,t)$ (t here is time) is given by

$$\mathbf{B} = \mathbf{B}_0 + \delta\mathbf{B} = \nabla(\psi_0 + \delta\psi) \times \nabla(\alpha_0 + \delta\alpha).$$

In this paper, we employ another form of magnetic perturbation; introducing the parallel component of the vector potential $A_\parallel$, the magnetic perturbation is given by $\delta\mathbf{B} = \nabla A_\parallel \times \mathbf{b}_0$. Here, we denote $\mathbf{b} = \mathbf{B}/B_0$ and $\mathbf{b}_0 = \mathbf{B}_0/B_0$. The vector potential $A_\parallel$ and the pair $\delta\psi$ and $\delta\alpha$ are related through the relations

$$\frac{\partial A_\parallel}{\partial \alpha_0} = -\mathbf{b}\cdot\nabla\delta\psi \tag{1}$$

and

$$\frac{\partial A_\parallel}{\partial \psi_0} = \mathbf{b}\cdot\nabla\delta\alpha. \tag{2}$$

Note that the perpendicular component of the vector potential $A_\perp$ is taken to be zero in this paper.

We first separate the distribution functions of the ions and the electrons into the equilibrium part and the fluctuation (the δ_f part)[20] as $f_i = f_{0i} + \delta f_i$ and $f_e = f_{0e} + \delta f_e$, where f_{0i} and f_{0e} are the ion and the electron equilibrium distribution function. The electron drift kinetic equation[21,22] is given by

$$\frac{d\delta f_e}{dt} = -\left(v_\parallel \frac{\delta\mathbf{B}}{B_0} + \mathbf{v}_E\right)\cdot\nabla f_{0e} + \left[ev_\parallel E_\parallel + v_\parallel \frac{\delta\mathbf{B}}{B}\cdot\nabla(\mu B) + \frac{cm_e v_\parallel^2 \mathbf{b}}{B}\times(\mathbf{b}\cdot\nabla)\mathbf{b}\cdot\nabla\Phi\right]\frac{\partial f_{0e}}{\partial\varepsilon}, \tag{3}$$

where $d/dt = \partial_t + (v_\parallel\mathbf{b} + \mathbf{v}_E + \mathbf{v}_d)\cdot\nabla$. The electron equilibrium distribution function is defined by $[\partial_t + (v_\parallel\mathbf{b}_0 + \mathbf{v}_d)\cdot\nabla]f_{0e} = 0$. The $E\times B$ drift velocity is given by $\mathbf{v}_E = c\mathbf{B}_0\times\nabla\Phi/B_0^2$, and the electron gradient-B drift and the electron curvature drift in low-β plasmas are given by $\mathbf{v}_d = (m_e\Omega_{ce}B_0^2)^{-1}(m_e v_\parallel^2 + \mu B_0)\mathbf{B}_0\times\nabla B_0$ (e is the unit charge, c is the speed of light, m_e is the electron mass, and $\Omega_{ce} = -eB_0/m_e c$ is the electron cyclotron frequency). Here, the magnetic moment is given by $\mu = m_e v_\perp^2/2B$ and the kinetic energy is given by $\varepsilon = \mu B + m_e v_\parallel^2/2$, where the parallel and perpendicular particle velocities are given by $v_\parallel$ and $v_\perp$, respectively (we have taken the magnetic moment μ and the kinetic energy ε as independent variables). Note in Eq. (3),

$$E_\parallel \equiv -\nabla_\parallel\Phi_{\text{eff}} = -\nabla_\parallel\Phi - c^{-1}\partial_t A_\parallel = -\nabla_\parallel\Phi + \nabla_\parallel\Phi_{\text{ind}}$$

contains both the electrostatic part and the induction part, and we introduce the *induction* potential Φ_{ind} and the *effective* potential Φ_{eff}, with Φ being the nominal electrostatic potential. In deriving Eq. (3), the conventional gyrokinetic ordering[21] is employed (the equilibrium electrostatic potential is taken to be zero). Note that all the perturbed quantities in the drift kinetic equation do not have finite Larmor radius contributions.

We further separate[10] δf_e into the adiabatic response and the nonadiabatic response. As in Ref. 12, the expansion parameter is

$$\frac{\omega}{k_\parallel v_\parallel} \sim \frac{v_A}{\sqrt{2}v_{\text{the}}} = \left(\frac{m_e}{\beta_e m_i}\right)^{1/2} = \delta_m,$$

where m_i is the ion mass, $v_A = B_0/(4\pi m_i n_0)^{1/2}$ is the Alfven velocity (the equilibrium plasma density is given by n_0), and $v_{\text{the}} = (T_e/m_e)^{1/2}$ is the electron thermal velocity (T_e is the equilibrium electron temperature). Here $\beta_e = 4\pi p_{0e}/B_0^2$ is (note the difference from the conventional $8\pi p_{0e}/B_0^2$) the ratio between the equilibrium electron pressure $p_{0e} = n_0 T_e$ and the magnetic pressure.

Keeping the terms proportional to $v_\parallel$ in Eq. (3), δf_e can be written as the combination of the lowest-order solution and the nonadiabatic contribution δh_e,

$$\delta f_e = -e\Phi_{\text{eff}}\frac{\partial f_{0e}}{\partial\varepsilon} + \delta\psi\frac{\partial f_{0e}}{\partial\psi_0} + \delta\alpha\frac{\partial f_{0e}}{\partial\alpha_0} + \delta h_e, \tag{4}$$

where we have employed Eqs. (1) and (2) to obtain the lowest-order solution δf_e in scalar form. Intuitively, the first term in Eq. (4) can be understood from the Boltzmann relation[23] with isothermal electrons along the magnetic field line, where we obtain

$$f_e = f_{0e}e^{(e\Phi_{\text{eff}}/T_e)} + \delta h_e \approx f_{0e} + (e\Phi_{\text{eff}}/T_e)f_{0e} + \delta h_e,$$

where a Taylor expansion is applied [then, we can denote $\delta f_e = (e\Phi_{\text{eff}}/T_e)f_{0e} + \delta h_e$]. As a result, the effective potential is expanded as $\Phi_{\text{eff}} = \Phi_{\text{eff}}^{(0)} + \Phi_{\text{eff}}^{(1)}$. The electron adiabatic re-

sponse is caused by the fast electron motion parallel to the magnetic field due to their small inertia; taking δ_m as an expansion parameter is a natural choice. The second term and the third term in Eq. (4) originated from the inhomogeneity in the equilibrium density and temperature profiles, as well as in the equilibrium magnetic field.

By substituting Eq. (4) and taking the moment of the electron drift kinetic equation (3), the continuity equation for the fluid electron is given by

$$\frac{\partial \delta n_e}{\partial t} = -(\mathbf{B}_0 + \delta\mathbf{B}) \cdot \nabla \frac{n_0 \delta u_{\parallel e}}{B_0} - \mathbf{v}_E \cdot \nabla (n_0 + \delta n_e) - \frac{\mathbf{B}_0 \times \nabla B_0}{m_e \Omega_{ce} B_0^2} \cdot [\nabla (\delta p_{\perp e} + \delta p_{\parallel e}) - 2 n_0 e \nabla \Phi], \quad (5)$$

where the pressure terms, $p_{\perp e}$ and $p_{\parallel e}$ are given by

$$\delta p_{\perp e} = \int \mu B \, \delta f_e d^3 v = n_0 e \Phi_{\text{eff}} + \delta\psi \frac{\partial p_{0\perp e}}{\partial \psi_0} + \delta\alpha \frac{\partial p_{0\perp e}}{\partial \alpha_0} + \int \mu B \, \delta h_e d^3 v,$$

$$\delta p_{\parallel e} = \int m_e v_\parallel^2 \, \delta f_e d^3 v = n_0 e \Phi_{\text{eff}} + \delta\psi \frac{\partial p_{0\parallel e}}{\partial \psi_0} + \delta\alpha \frac{\partial p_{0\parallel e}}{\partial \alpha_0} + \int m_e v_\parallel^2 \, \delta h_e d^3 v,$$

where $\int d^3 v$ is the integral over velocity space. The continuity equation, Eq. (5), is analogous to that of Parker and Chen.[24,25] Note that the last terms (the integrals) in $\delta p_{\perp e}$ and $\delta p_{\parallel e}$ are higher-order terms. They enter the system by taking the moment of the nonadiabatic kinetic response δh_e (see below).

To obtain the magnetic perturbation, we use Faraday's law,

$$\frac{\partial A_\parallel}{\partial t} = c \nabla_\parallel (\Phi_{\text{eff}} - \Phi). \quad (6)$$

Instead of solving Eqs. (1) and (2), the following magnetic field equation is solved to determine $\delta\psi$ and $\delta\alpha$ in the Clebsch form:[26]

$$\frac{\partial \delta\psi}{\partial t} = -\mathbf{v}_{\Phi_{\text{ind}}} \cdot \nabla \delta\psi + c \frac{\partial \Phi_{\text{ind}}}{\partial \alpha_0}, \quad (7)$$

$$\frac{\partial \delta\alpha}{\partial t} = -\mathbf{v}_{\Phi_{\text{ind}}} \cdot \nabla \delta\alpha - c \frac{\partial \Phi_{\text{ind}}}{\partial \psi_0}, \quad (8)$$

where $\mathbf{v}_{\Phi_{\text{ind}}} = c\mathbf{B}_0 \times \nabla (\Phi_{\text{ind}} / B_0^2)$. Note that Eqs. (7) and (8) are derived from the time derivatives of the conditions $\mathbf{b} \cdot \nabla \psi = 0$ and $\mathbf{b} \cdot \nabla \alpha = 0$, respectively. The nonlinear terms in Eqs. (7) and (8) correspond to $\nabla \delta\psi \times \nabla \delta\alpha$ of the magnetic field in the Clebsch form. The dynamical equations, Eqs. (3)–(8), are time-advanced in the simulations [however, in the simulation of this paper we use the approximate relation $\delta\psi = A_\parallel R$,[27] which is consistent with Eq. (1) in the limit when the magnetic field is purely toroidal].

After the dynamical equations, the following three field equations are solved at each numerical time step of the GTC simulation. These are the gyrokinetic Poisson equation[6,7] for the electrostatic potential Φ,

$$-\frac{\tau}{\lambda_d^2} (\Phi - \tilde{\Phi}) = -4\pi e (\delta \bar{n}_i - \delta n_e) \quad (9)$$

("$\bar{\ }$" representing the gyroaveraging) the lowest-order equation for the parallel electric field,

$$\frac{e \Phi_{\text{eff}}^{(0)}}{T_e} = \frac{\delta n_e}{n_0} - \frac{\delta\psi}{n_0} \frac{\partial n_0}{\partial \psi_0} - \frac{\delta\alpha}{n_0} \frac{\partial n_0}{\partial \alpha_0}, \quad (10)$$

and Ampere's law,

$$n_0 e \, \delta u_{\parallel e} = \frac{c}{4\pi} \nabla_\perp^2 A_\parallel + n_0 e \, \delta \bar{u}_{\parallel i}. \quad (11)$$

Here, $\tau = T_e / T_i$ is the ratio between the equilibrium electron temperature T_e and the equilibrium ion temperature T_i, and $\tilde{\Phi}$ is the *second* gyro-phase-averaged potential,[7] as a result of ion polarization density response. The second term on the right of Eq. (10) represents the isothermal electron response along the perturbed magnetic field. Equations (5)–(11) constitute the part of the hybrid model with the electron fluid, that is, the lowest-order system in the δ_m expansion (here "lowest" refers to the expansion in δf_e).

We now proceed to first order in the δ_m expansion by retaining the higher-order terms; we obtain the electron kinetic equation given by

$$\frac{d \delta h_e}{dt} = c \frac{\partial f_{0e}}{\partial \psi_0} \frac{\partial \Phi}{\partial \alpha_0} - c \frac{\partial f_{0e}}{\partial \alpha_0} \frac{\partial \Phi}{\partial \psi_0} - \frac{\partial f_{0e}}{\partial \psi_0} \frac{\partial \delta\psi}{\partial t} - \frac{\partial f_{0e}}{\partial \alpha_0} \frac{\partial \delta\alpha}{\partial t} - (\mathbf{v}_E + \mathbf{v}_d) \cdot \nabla \left(\frac{\partial f_{0e}}{\partial \psi_0} \delta\psi + \frac{\partial f_{0e}}{\partial \alpha_0} \delta\alpha \right) + e \frac{\partial f_{0e}}{\partial \varepsilon} \frac{\partial \Phi_{\text{eff}}}{\partial t} - (\mathbf{v}_E + \mathbf{v}_d) \cdot \nabla \left(\frac{\partial f_{0e}}{\partial \varepsilon} e \Phi_{\text{ind}} \right). \quad (12)$$

The time derivative terms $\partial_t \Phi_{\text{eff}}$, $\partial_t \delta\psi$, and $\partial_t \delta\alpha$ are given by Eqs. (5), (7), and (8). Using Eq. (4) and the subsequent expansion, we obtain the relation

$$\frac{e \Phi_{\text{eff}}^{(1)}}{T_e} = -\frac{\delta n_e^{(1)}}{n_0} \quad (13)$$

to obtain $\Phi_{\text{eff}} = \Phi_{\text{eff}}^{(0)} + \Phi_{\text{eff}}^{(1)}$, which then enters Eq. (6). In Eqs. (9), (11), and (13), $\delta \bar{n}_i$, $\delta \bar{u}_{\parallel i}$, and $\delta n_e{}^{(1)}$ are given by $\delta \bar{n}_i = (1/n_0) \int \delta f_i d^3 v$, $\delta \bar{u}_{\parallel i} = (1/n_0) \int v_\parallel \delta f_i d^3 v$, and $\delta n_e{}^{(1)} = (1/n_0) \int \delta h_e d^3 v$. However, we do not take the moment of δh_e for $\delta u_{\parallel e}$ [see Eq. (11)].

The δf gyrokinetic equation[21,22] is solved for the kinetic ions

$$\frac{d \delta f_i}{dt} = -\left(v_\parallel \frac{\delta \mathbf{B}}{B_0} + \mathbf{v}_E \right) \cdot \nabla f_{0i} + \left[-e v_\parallel E_\parallel + v_\parallel \frac{\delta \mathbf{B}}{B} \cdot \nabla (\mu B) + \frac{c m_i v_\parallel^2 \mathbf{b}}{B} \times (\mathbf{b} \cdot \nabla) \mathbf{b} \cdot \nabla \Phi \right] \frac{\partial f_{0i}}{\partial \varepsilon}, \quad (14)$$

where the ion equilibrium distribution function is defined by $[\partial_t+(v_\parallel \mathbf{b}_0+\mathbf{v}_d)\cdot\nabla]f_{0i}=0$ and the ion gradient-B and curvature drift is given by $\mathbf{v}_d=(m_i\Omega_{ci}B_0^2)^{-1}(m_iv_\parallel^2+\mu B_0)\mathbf{B}_0\times\nabla B_0$ ($\Omega_{ci}=eB_0/m_ic$ is the ion cyclotron frequency). Here, the magnetic moment is given by $\mu=m_iv_\perp^2/2B$ and the kinetic energy is given by $\varepsilon=\mu B+m_iv_\parallel^2/2$. All the perturbed quantities in Eq. (14) are gyro-phase-averaged values.

As noted in the Introduction, the model is not derived for studying tearing parity modes. At the mode rational surfaces where $k_\parallel$ vanishes, the small expansion parameter $\delta_m\sim(\omega/k_\parallel v_{\mathrm{the}})$ diverges (if ω does not vanish). The gyrokinetic model also excludes the fast compressional Alfven wave. However, compressible magnetic fluctuations (slow modes) could be treated by solving a perpendicular Ampere's law, which is simply a perpendicular force balance equation in the limit of long wavelength and low frequency.[28]

We solve Eqs. (5), (6), (9), and (11) to study the Alfven oscillations, and solve Eqs. (5), (6), (9), (11), and (14) in cases with kinetic ions. We do not solve Eq. (12) in this paper.

III. SHEAR ALFVEN WAVE OSCILLATIONS AND CONTINUUM DAMPING

In this section, we verify shear Alfven wave propagation by reducing the hybrid model. We set $\delta n_i=0$ in Eq. (9) and $\delta u_{\parallel i}=0$ in Eq. (11). By linearizing Eqs. (5), (6), (9), and (11) and combining them together, we obtain a hyperbolic equation

$$\frac{\partial^2\nabla_\perp^2\Phi}{\partial t^2}=v_A^2\nabla_\parallel^2\nabla_\perp^2(1-\rho_s^2\nabla_\perp^2)\Phi. \tag{15}$$

Note that, by an expansion in the long-wavelength limit, the left side of Eq. (9) becomes[6] $-\tau\lambda_d^{-2}(\Phi-\tilde{\Phi})\sim(\rho_s/\lambda_d)^2\nabla_\perp^2\Phi$, where λ_d is the Debye length, recovering the $\nabla_\perp^2$ operator of the nominal Poisson equation. Here, $\rho_s=m_ic_s/ceB_0$ is the ion Larmor radius at the electron temperature, where $c_s=\sqrt{T_e/m_i}$ is the sound speed. Assuming a homogeneous plasma and Fourier transforming Eq. (15) in the form $\Phi\sim\exp(i\mathbf{k}\cdot\mathbf{r}-i\omega t)$, we obtain the shear Alfven wave dispersion relation

$$\omega^2=v_A^2k_\parallel^2(1+\rho_s^2k_\perp^2), \tag{16}$$

where $k_\perp$ is the component of the wave vector $\mathbf{k}$ perpendicular to the equilibrium magnetic field. An additional $\rho_s^2k_\perp^2$ term appears on top of the nominal shear Alfven dispersion relation[29,30] due to the polarization density response in the Poisson equation (9). Note that the eigenmode that can be obtained from Eq. (16) only applies for homogeneous plasmas with a uniform magnetic field. In real three-dimensional systems, the Alfven velocity v_A varies spatially as a function of the equilibrium magnetic field strength B_0 and the equilibrium density n_0 ($k_\parallel$ varies spatially as well with finite magnetic shear), and gives rise to the Alfven continuum where eigenmodes and eigenfrequencies are not discrete.

In the GTC simulations, we first verify that the dispersion relation Eq. (16) is satisfied. We verify the $k_\parallel$ dependence of the frequency as well as the v_A (or β_e) dependence. Equations (5), (6), (9), and (11), which are used to derive the dispersion relation, are time-advanced. We also demonstrate the linear phase mixing of the Alfven wave known as continuum damping.[31–33]

The plasma parameters employed for the simulation are that of the "Cyclone DIII-D base case parameter set,"[34] with a toroidal magnetic field of $1.91T$. The plasma size is given by the major radius $R=93.2$ cm and the minor radius $a=33.3$ cm. An annular simulation domain is employed ($r_{\min}=0.1a$ and $r_{\max}=0.9a$). The safety factor varies within the range $0.87\leqslant q\leqslant 2.62$. The magnetic field strength changes spatially proportional to the inverse of the major radius as $|B|\sim 1/R$. The density gradient is chosen to be small so that there is no instability drive, $\kappa_n=-R[d\log(n)/dr]=0.01$. Here, $\beta_e=1.0\%$ is taken. The geometry we employ is toroidal, but the poloidal cross section remains circular. A total of 37936 grid points per poloidal plane are taken with the logically nonrectangular mesh.[16] In the toroidal direction, a total of 64 planes were employed with the global field aligned mesh[35,36] we employ in GTC. Homogeneous Dirichlet boundary conditions are taken for Φ, δn_e, Φ_{eff}, and $A_\parallel$. As an initial condition for the vector potential $A_\parallel$ (at $t=0$), we take the form

$$A_\parallel=A_0\sin\left(\pi\frac{r-r_{\min}}{r_{\max}-r_{\min}}\right)\exp(im\theta-in\zeta). \tag{17}$$

Here m (n) stands for the poloidal (toroidal) mode number.

Shown in Fig. 1(a) is the amplitude of the vector potential $A_\parallel$ as a function of time. Figure 1(a) is obtained from the *linear runs*; we have selected a single $n=5$ mode with all m harmonics. In Fig. 1(a), the Fourier mode with $m=4$, $n=5$ is shown [we have chosen $m=4$, $n=5$ in Eq. (17) for the initial condition]. The oscillatory behavior in Fig. 1(a) is the manifestation of the Alfven wave propagation. As predicted by the theory,[31,37,38] the Alfven wave experiences continuum damping,[32,33] demonstrating inverse time dependence $\sim 1/t$ of the envelope decay.[37] Magnetic field inhomogeneity gives rise to the Alfven continuum spectrum[32,33] and allows phase mixing. To see whether the damping is $1/t$-like or exponential, we fit the envelope of the oscillatory behavior. Shown in Fig. 1(b) is the absolute value of the $A_\parallel$ Fourier components. The dashed curves are from the $1/t$ fit and the long dashed line is from the exponential fit. As we see, the $1/t$ fit is favorable in the initial phase, suggesting the continuum damping.

In Fig. 2, we investigate the $k_\parallel$ dependence of the frequency. In Fig. 2, the initial condition Eq. (17) is given by $m=7$, $n=5$ (simulations of Fig. 1 and Fig. 2 are different). To verify the $k_\parallel$ dependence, recalling the relation $k_\parallel=\mathbf{b}_0\cdot\nabla=(m-nq)/qR$ in a large aspect ratio tokamak (R is the major radius), the dispersion relation for $k_\perp^2\rho_s^2\ll 1$ is given by

$$\omega=k_\parallel v_A=\frac{m-nq}{qR}v_A. \tag{18}$$

Shown in Fig. 2(a) are the absolute values of $A_\parallel$ for the $4\leqslant m\leqslant 7$ modes as a function of time, where $n=5$ is taken as

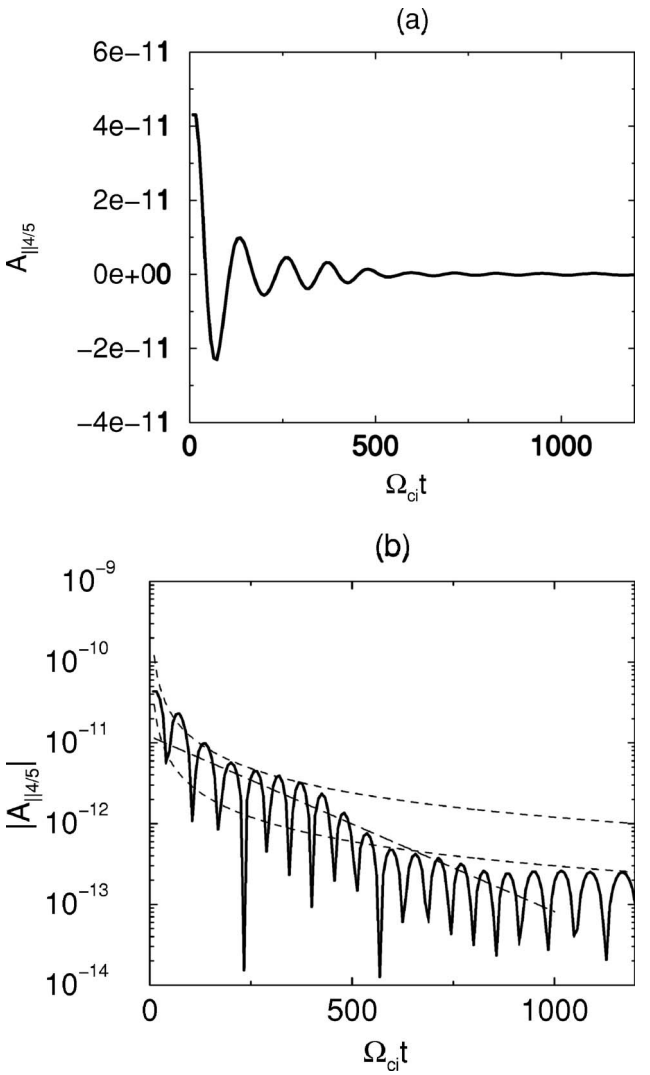

FIG. 1. Alfven oscillation demonstrated by the $m/n=4/5$ mode of the vector potential $A_\|$. (a) The $A_\|$ evolution versus time. The mode is diagnosed at the $q=1.4$ surface (at the midplane $r/a=0.5$). (b) The absolute value $|A_\|$| evolution versus time. The dashed curves are a $1/t$ decay, while the long dashed line is an exponential decay. Here, $\beta_e=1.0\%$ is taken.

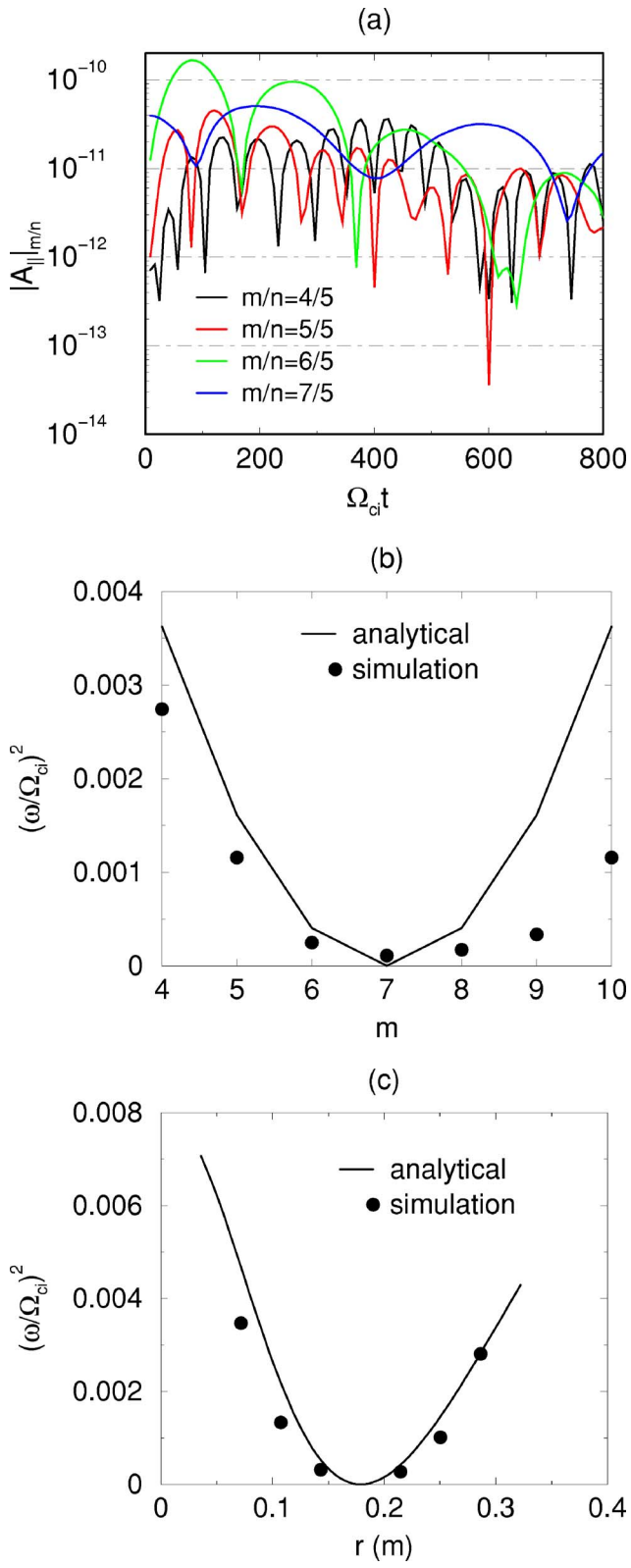

FIG. 2. (Color online) (a) The amplitudes of the vector potential $A_\|$ as a function of time. (b) Real frequency of the shear Alfven wave as a function of poloidal mode number m. (c) Real frequency of the shear Alfven wave as a function of the minor radius. Here, the mode numbers $m=7$ and $n=5$ are fixed but the location of the Fourier diagnosis is varied. Here, $\beta_e=1.0\%$ is taken.

in Fig. 1(a) (note $0.87<q<2.62$). All the modes are diagnosed at the $q=1.4$ surface. As we change the m values (so that m/n becomes closer to $q=1.4$), $k_\|$ and thus ω become smaller. This tendency is captured in Fig. 2(b) in comparison with the solid curve obtained from the analytical dispersion relation. The deviation from the theoretical prediction becomes large as the resonating mode rational surface moves far from the $q=1.4$ surface.

We have also changed the radial location of the diagnosis plane with m and n fixed. Shown in Fig. 2(c) is the real frequency as a function of the radial location. We plot ω^2 in the conventional way (the simulation manifests both the positive and the negative frequencies). In Figs. 2(a)–2(c), $\beta_e=1.0\%$ is taken.

In Fig. 3, we present the β_e dependence of the frequency. As a reminder, the Alfven velocity is $v_A=B_0/(4\pi m_i n_0)^{1/2} \propto \beta_e^{-1/2}$ (note that $\beta_e=c_s^2/v_A^2$). In Fig. 3, the solid line is obtained from the analytical expression. This is the evidence of shear Alfven wave propagation in our initial value approach gyrokinetic simulation.

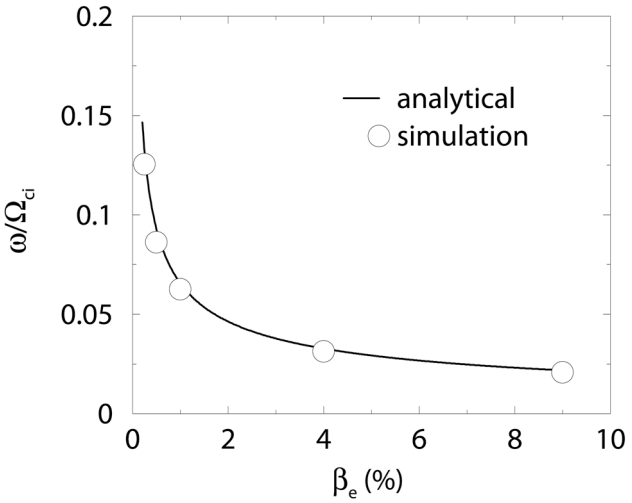

FIG. 3. The Alfven frequency as a function of β_e. The solid line is obtained from the analytical expression in the $k_\perp \rho_s \ll 1$ limit.

IV. TOROIDAL EFFECTS ON THE ALFVEN FREQUENCY

In toroidal geometry, the poloidal variation of the magnetic field induces mode coupling of neighboring poloidal mode numbers. The toroidicity is known to break the Alfven continuum and to generate the so-called frequency gap.[2] From the hybrid model, combining Eqs. (5), (6), (9), and (11), and by dropping the Φ_{eff} term (in the ideal MHD limit with $E_\parallel=0$), we obtain Eq. (2) of the work by Fu and Van Dam,[39] which is the quasineutrality equation in toroidal geometry. Note that the coefficient ρ_s^2 on the left of the gyrokinetic Poisson equation contains the $1/R$ variation of the magnetic field strength [see Eq. (9), $-\tau\lambda_d^{-2}(\Phi-\tilde{\Phi}) \sim (\rho_s/\lambda_d)^2\nabla_\perp^2\Phi$]. The magnetic field inhomogeneity through ρ_s^2 gives rise to the poloidal mode coupling and thus the frequency gap.

According to the analysis by Fu and Van Dam,[39] for two dominant poloidal mode numbers, for the charge continuity equation to give nontrivial solutions, the continuum frequency in the toroidal geometry is given by

$$\omega_\pm^2 = \frac{k_{\parallel m}^2 v_A^2 + k_{\parallel m+1}^2 v_A^2 \pm \sqrt{(k_{\parallel m}^2 v_A^2 - k_{\parallel m+1}^2 v_A^2)^2 + 4\epsilon^2 x^2 k_{\parallel m}^2 v_A^2 k_{\parallel m+1}^2 v_A^2}}{2(1-\epsilon^2 x^2)}, \tag{19}$$

where $x=r/a$, and $\epsilon=a/R$ is the inverse aspect ratio, and $k_{\parallel m}$ and $k_{\parallel m+1}$ are for the poloidal mode numbers m and $m+1$, respectively [see Eq. (18)]. Here, the $\pm$ signs signify the two separated branches shown in Fig. 4. Figure 4 depicts the shear Alfven frequency as a function of the minor radius. Note that the ordinate is normalized by the Alfven frequency at the magnetic axis ($r=0$). The dashed curves are the continuum frequency in the cylindrical limit. The solid lines are from Eq. (16), the continuum frequency in a torus. The lower (upper) boundary of the upper (lower) curve is signified by the dashed lines at $\omega/\omega_a=0.389$ ($\omega/\omega_a=0.299$), where $\omega_a = v_A/q(0)R$. As a consequence, the frequency gap appears with $0.299<\omega/\omega_a<0.389$ (in terms of cyclotron frequency, $0.0171<\omega/\Omega_{ci}<0.0225$). The toroidicity induced Alfven eigenmode (TAE)[2] can reside within this frequency gap. Figure 4 is a recapitulation of Fig. 1 of Ref. 39.

While Fu and Van Dam[39] used an eigenvalue approach, we take an initial value approach. The frequency spectrum is obtained by Fourier transforming the time series data. For the simulation we take exactly the same parameters as in Ref. 39 [the safety factor profile is given by $q=1+(r/a)^2$; aspect ratio is given by $\epsilon=0.375$]. The major radius is chosen to be half the size of Sec. III, $R=46.6$ cm, and we set $\beta_e=1.0\%$. We examine the two poloidal harmonics $m=1$ and 2 with a toroidal mode of $n=1$. The initial condition for the vector potential $A_\parallel$ at $t=0$ is given by a combination of the $m=1$ and 2 modes [see Eq. (17)].

Shown in Fig. 5(a) are the amplitudes of the $m=1$ and 2

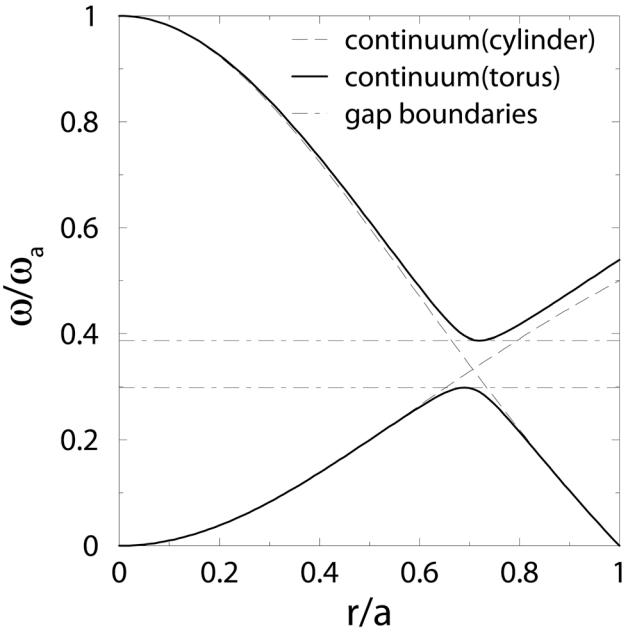

FIG. 4. Shear Alfven frequency as a function of the radial location. The dashed curves are the continuum frequencies for the cylindrical limit, for $m=1$ and 2 modes. The solid lines are for the continuum frequency with the toroidal geometry effect. The lower (upper) boundary of the upper (lower) curve is at $\omega/\omega_a=0.389$ ($\omega/\omega_a=0.299$). Correspondingly, the frequency gap (the forbidden frequency range) appears with the range $0.299<\omega/\omega_a<0.389$. The figure is a recapitulation of Fig. 1 of Ref. 39.

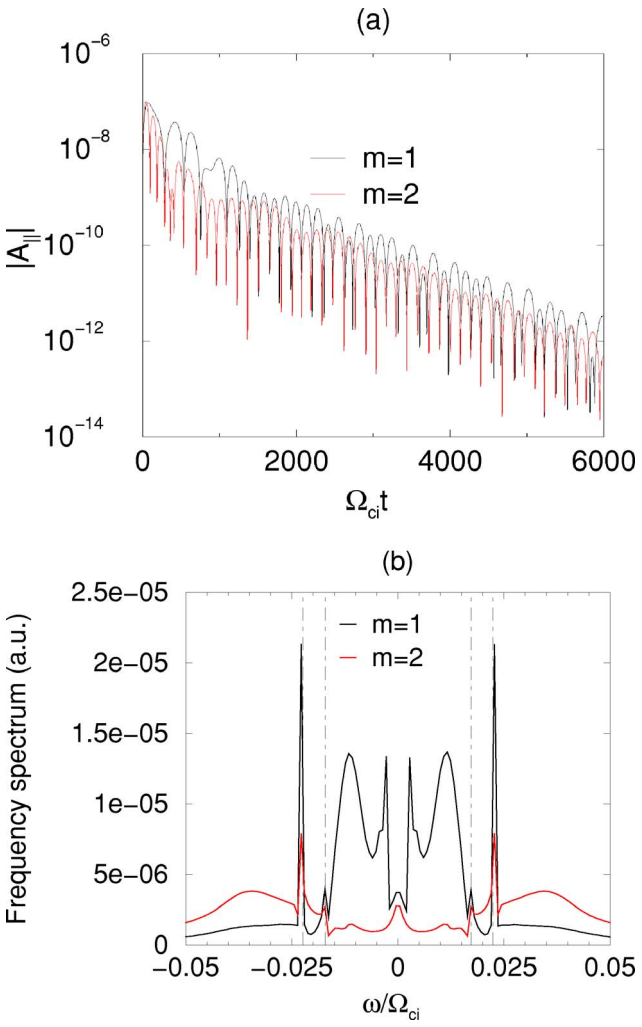

FIG. 5. (Color online) (a) The Fourier components of the amplitude of the vector potential $A_\parallel$ as a function of time. The black curve is for the $m=1$ mode; the red curve is for the $m=2$ mode. The mode amplitude is diagnosed at the midplane where $r/a=0.5$. (b) The frequency spectrum obtained from the time series of Fig. 5(a) (black for $m=1$, red for $m=2$). For $m=1$, the two broad peaks at $\omega/\Omega_{ci}=\pm 0.0112$ correspond to the continuous spectrum and the sharp peaks at $\omega/\Omega_{ci}=\pm 0.0171$ ($\omega/\omega_a=\pm 0.299$) and $\omega/\Omega_{ci}=\pm 0.0225$ ($\omega/\omega_a=\pm 0.389$) correspond to the lower and the upper limits of the continuous (torus) curves in Fig. 4. For $m=2$, the two broad peaks at $\omega/\Omega_{ci}=\pm 0.0337$ correspond to the continuum spectrum. The sharp peaks for $m=2$ are found at $\omega/\Omega_{ci}=\pm 0.0171$ and ± 0.0225 that are exactly the same as for $m=1$.

components of $A_\parallel$ versus time. The frequency spectrum is diagnosed at the midplane, where $r/a=0.5$ and thus $q=1.25$. Fourier transforming the time series in Fig. 5(a), we obtain the frequency spectrum in Fig. 5(b). The broad peaks at $\omega/\Omega_{ci}=\pm 0.0112$ correspond to the continuous spectrum (with the finite width suggesting the damping). The sharp peaks at $\omega/\Omega_{ci}=\pm 0.0171$ and ± 0.0225 (dotted-dashed lines) correspond to accumulation points[3] (the lower and the upper limits of the curves in Fig. 4). Similarly, the red curves in Figs. 5(a) and 5(b) are for the $m=2$ mode. As before, the broad peaks at $\omega/\Omega_{ci}=\pm 0.0337$ in Fig. 5(b) correspond to the continuous spectrum. The mode with the frequency at the accumulation point survives much longer than the continuum part. Note that we find sharp peaks for $m=2$ at $\omega/\Omega_{ci}=\pm 0.0171$ and ± 0.0225 that are exactly at the same positions in Fig. 5(b) as for the $m=1$ case. This feature, suggesting the correlation of different m, is due to the poloidal mode coupling. The generation of the frequency gap is seen in the range $0.0171<\omega/\Omega_{ci}<0.0225$, which corresponds exactly to $0.299<\omega/\omega_a<0.389$ in Fig. 4 ($\Omega_{ci}/\omega_a=17.4$). Interestingly, the sharp peaks (that correspond to the accumulation points) stay at the same frequencies even when we change the diagnosis plane, indicating the formation of a global mode.

As a reminder, the simulations discussed in the previous section (Figs. 1 and 2) do contain the toroidal effects. However, with the Fourier modes and the q-profile we have chosen, the width of the frequency gap is quite small. Note that the simulation time is not long enough as in Fig. 5; the oscillatory behavior is dominated by the cylindrical-like initial condition of Eq. (17).

The TAE frequencies should reside between the two sharp peaks (within the gap). One approach to simulate the TAE is to perturb the magnetic field at $t=0$ with an expected eigenmode structure; the other approach is by energetic particle drive whose velocity is comparable to the local Alfven velocity. For the first method, we need to carefully choose the initial condition. The second can be done either by the loading of a non-Maxwellian distribution function with a high-energy tail, or adding a second species such as fusion reaction generated α particles. Both methods are beyond the scope of this paper and we plan to report on them in the future.

V. PERPENDICULAR PROPAGATION OF SHEAR ALFVEN WAVES

We investigate finite "$k_\perp$" effects on the shear Alfven wave. The perpendicular wave component $k_\perp\rho_s$ in the dispersion relation Eq. (16) arises from the ion polarization drift in the gyrokinetic Poisson equation (9). Being different from the ideal MHD shear Alfven wave, the kinetic Alfven wave[18,19] can propagate across the equilibrium magnetic field. Incorporating the kinetic ion equation (14), the dispersion relation in the drift-kinetic limit is given by

$$\left(\frac{\omega^2}{k_\parallel^2 v_A^2}-1\right)[1+\tau+\tau\zeta_i Z(\zeta_i)]=k_\perp^2\rho_s^2. \tag{20}$$

Note that in the presence of kinetic electrons, the first term "1" in the square brackets will be replaced by $1+\zeta_e Z(\zeta_e)$. Here $Z(\zeta)$ is the plasma dispersion function,[40] $\zeta_i=\omega/(k_\parallel v_{\mathrm{thi}})$ with v_{thi} being the ion thermal velocity, and $\zeta_e=\omega/(k_\parallel v_{\mathrm{the}})$. In the $\zeta_i\gg 1$ limit (since the phase velocity is much larger than the ion thermal velocity), the terms inside the square brackets of Eq. (20) become $1+\tau+\tau\zeta_i Z(\zeta_i)=1-\tau\zeta_i^{-2}/2$. Thus the kinetic ion contribution is negligible since $\zeta_i^{-2}\ll 1$. The finite $k_\perp$ contribution in this simulation is due to the ion polarization drift.

Shown in Fig. 6 is the real frequency ω versus the poloidal mode number m. We have chosen poloidal and the toroidal modes m and n so that $k_\parallel=(m/q-n)/R$ is kept constant and only $k_\perp\sim m/r$ varies. The toroidal mode numbers chosen are $5\leqslant n\leqslant 25$ with $m=nq-1$. The Fourier modes are diagnosed on the $q=1.4$ ($r/a=0.5$) surface as before. Since

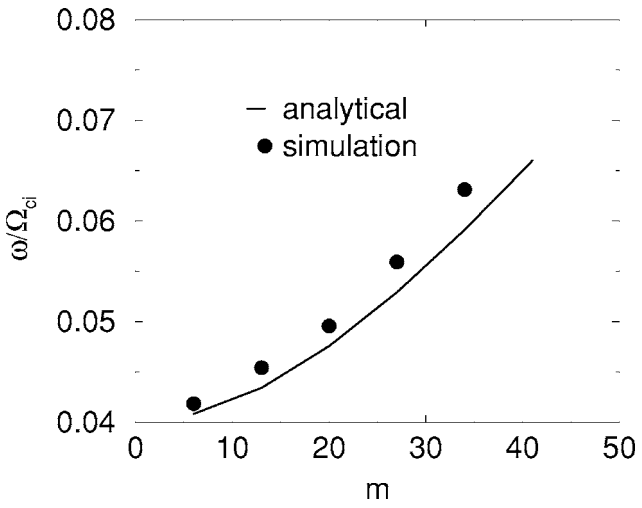

FIG. 6. Real frequency of kinetic shear Alfven wave as a function of poloidal mode number m. Here, $m=40$ corresponds to $k_\perp \rho_s = 0.8$. The corresponding dispersion relation is shown as a solid line.

we aim to elucidate the $k_\perp$ effect, a relatively small plasma size is taken [major radius $R=46.6$ cm and minor radius $a=16.7$ cm] so that the $k_\perp \rho_s$ term in Eq. (16) quickly becomes large. In Fig. 6, $\beta_e = 0.25\%$ is chosen.

As before, the initial condition for the vector potential $A_\parallel$ (at $t=0$) is given by Eq. (17) (sinusoidal function for the radial profile) to suppress the contribution of the radial wavevector component k_r (note that $\mathbf{k}_\perp = \mathbf{k}_\mathbf{r} + \mathbf{k}_\theta$).

The solid curve in Fig. 6 is obtained analytically employing $\omega = v_A k_\parallel \sqrt{k_\perp^2 \rho_s^2 + 1}$. The real frequency obtained from the simulation results compares favorably with the analytical curve, supporting the observation of perpendicular wave propagation (or kinetic Alfven waves).

VI. FINITE BETA STABILIZATION OF ITG AND ONSET OF ALFVENIC ITG

In this section, we investigate electromagnetic effects on the ion temperature gradient (ITG) mode. In the tokamak core region, due to the auxiliary heating, the ion temperature gradient exceeds the density gradient and induces the instability known as the ion temperature gradient (ITG) mode,[41] which is believed to be the predominant drive for the ion energy transport. In the presence of electromagnetic effects, due to the coupling of the ion acoustic wave and the Alfven wave, the linear growth rate of the ITG mode is expected to decrease (finite-β stabilization).[42,43] Further, at a critical value of the plasma pressure (below the ideal MHD threshold), excitations of new branches of electromagnetic modes, which are the Alfvenic ion temperature gradient mode (AITG) or the kinetic ballooning mode (KBM), are predicted.[3–5]

The parameters used in this section are toroidal magnetic field 1.91 T, equilibrium ion temperature $T_i = 2500$ eV, and equilibrium ion density 4.6×10^{19} m^{-3}. The plasma size is given by the major radius $R=46.6$ cm and the minor radius $a=16.7$ cm. The density gradient and the ion temperature gradient are given by $\kappa_n = -R[dlog(n)/dr] = 2.00$ and $\kappa_{ti} = -R[dlog(T_i)/dr] = 14.0$. As before, the growth rates and the real frequencies are diagnosed at the $q=1.4$ surface ($0.87 < q < 2.62$).

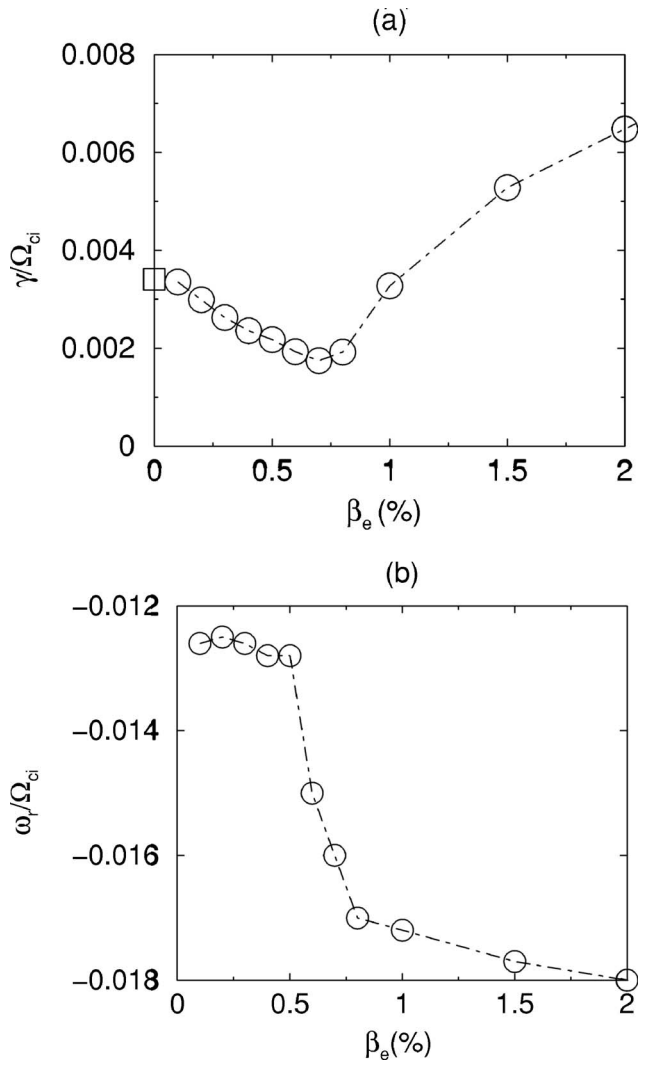

FIG. 7. (a) The β_e dependence of finite beta modified ITG linear growth rates for $n=10$. The square point is obtained from the electrostatic model with adiabatic electrons. (b) Real frequency of the finite-β modified ITG mode.

The linear growth rate versus the β_e value is shown in Fig. 7(a), demonstrating finite-β stabilization[42,43] for the $n=10$ mode and the onset of the AITG mode. Figure 7(b) shows the dependence of the real frequency on β_e. The square point at $\beta_e = 0$ is obtained from the electrostatic simulation with adiabatic electrons. The Fourier modes included (filtered) in this simulation are all the m modes and a single $n=10$. In Fig. 8, the linear eigenfunction of the finite-β modified ITG is shown for $\beta_e = 0.4\%$. The two contour plots are those on the $\zeta = 0$ poloidal plane. Note that the radial profile of Φ has even parity across the mode rational surfaces, while $A_\parallel$ has odd parity. The onset of the AITG below the ideal MHD critical limit requires a more detailed numerical analysis. Nonlinear simulation results have been presented;[44] a comprehensive parameter survey will be reported separately.

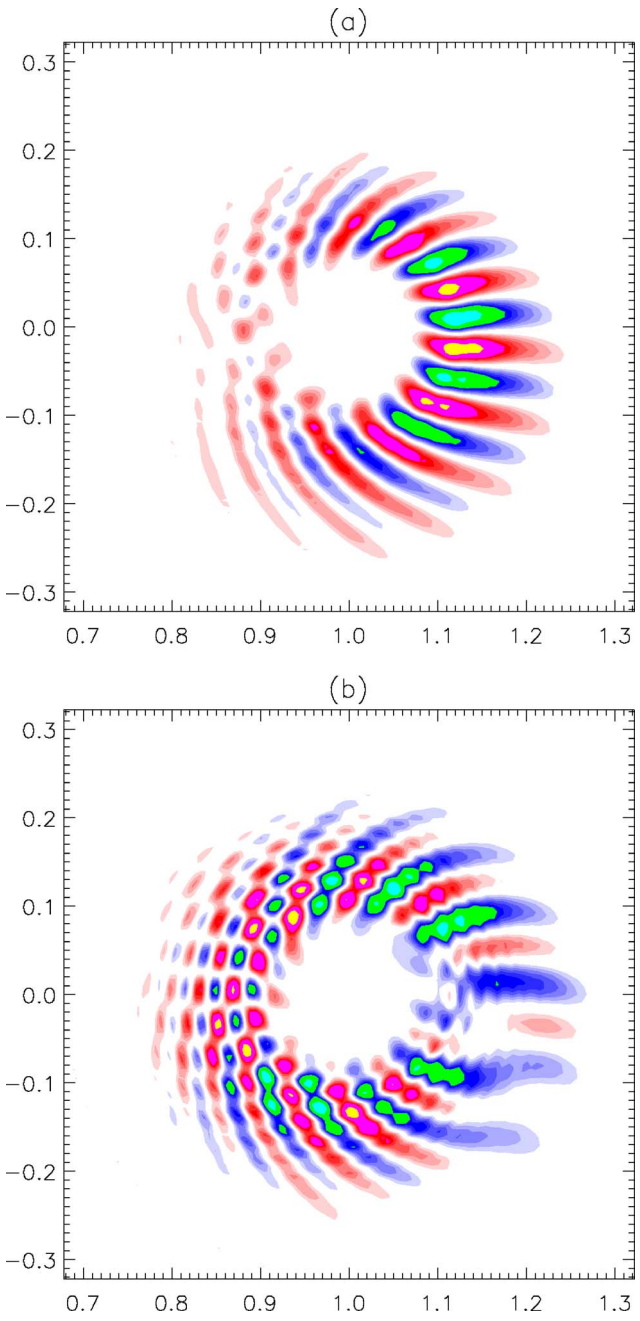

FIG. 8. (Color online) (a) Contour plot of the electrostatic potential Φ at toroidal angle $\zeta=0$. Red represents positive Φ values, while blue represents negative Φ values. (b) Contour plot of vector potential $A_{\parallel}$ at toroidal angle $\zeta=0$. Note that Φ has even parity and $A_{\parallel}$ has odd parity. Here, $\beta_e=0.4\%$.

VII. SUMMARY

In this paper, an electromagnetic simulation in global toroidal geometry is developed based on a fluid-kinetic hybrid electron model. The hybrid model solves for the adiabatic response in the lowest order and solves for the kinetic response in the higher orders, and preserves the linear and the nonlinear wave-particle interactions for the electrons. Employing a linearized version of the hybrid model in the electron fluid limit, continuum damping of the shear Alfven wave is demonstrated. Further, due to the toroidal effects, the frequency gap has been generated. The dependence of the Alfven frequency on finite $k_{\perp}$ (kinetic Alfven wave) is discussed. These results (capturing the continuum and the gap frequency) are uniquely obtained in an initial value approach (in contrast to the conventional eigenmode analysis) incorporating the gyrokinetic Poisson equation in a global tokamak geometry. This simulation method emerges as a promising tool not only for electromagnetic turbulence studies but also for investigation of kinetic effects on magnetohydrodynamic instabilities.

Future work will study excitation and nonlinear saturation mechanisms of the TAE mode. In burning plasmas, for example, the alpha particles excites the TAE, and the long-wavelength TAE mode can couple to shorter-wavelength microturbulence.

As a preliminary study for turbulence transport, the effect of finite-β on the ITG linear growth rate is shown. The finite-β stabilization and the onset of the AITG are demonstrated. A more comprehensive simulation (with the higher-order kinetic electron response) of the onset threshold and the saturation mechanism of the AITG mode[3,4] will be our near-term future work.

ACKNOWLEDGMENTS

The authors are grateful to L. Chen, T. S. Hahm, S. Hu, W. W. Lee, Y. Chen, V. K. Decyk, G. Y. Fu, N. Gorelenkov, F. L. Hinton, I. Holod, J. R. Johnson, P. Lauber, S. E. Parker, G. Rewoldt, M. N. Rosenbluth, and B. Scott for fruitful discussions. This work is supported by U.S. Department of Energy Grant No. DE-FG02-03ER54724, Cooperative Agreement No. DE-FC02-04ER54796, and in part by the SciDAC Center for Gyrokinetic Particle Simulation of Turbulent Transport in Burning Plasmas. Work by Y.N. was partially performed during his stay at the Princeton Plasma Physics Laboratory. Numerical simulations were performed using the IBM SP-5 supercomputers at the National Energy Research Supercomputing Center.

[1] Z. Lin, T. S. Hahm, W. W. Lee, W. M. Tang, and R. B. White, Science **281**, 1835 (1998).
[2] C. Z. Cheng, L. Chen, and M. S. Chance, Ann. Phys. (N.Y.) **161**, 21 (1985); C. Z. Cheng and M. S. Chance, Phys. Fluids **29**, 3695 (1986).
[3] F. Zonca, L. Chen, R. A. Santoro, and J. Q. Dong, Plasma Phys. Controlled Fusion **40**, 2009 (1998).
[4] G. Zhao and L. Chen, Phys. Plasmas **9**, 861 (2002).
[5] C. Z. Cheng, Phys. Fluids **25**, 1020 (1982).
[6] W. W. Lee, Phys. Fluids **26**, 556 (1983).
[7] W. W. Lee, J. Comput. Phys. **72**, 243 (1987).
[8] J. C. Reynders, Ph.D. dissertation, Princeton University (1992).
[9] J. C. Cummings, Ph.D. dissertation, Princeton University (1995).
[10] I. Manuilskiy and W. W. Lee, Phys. Plasmas **7**, 1381 (2000).
[11] W. W. Lee, J. L. V. Lewandowski, T. S. Hahm, and Z. Lin, Phys. Plasmas **8**, 4435 (2001).
[12] Z. Lin and L. Chen, Phys. Plasmas **8**, 1447 (2001).
[13] W. X. Wang, L. Chen, and Z. Lin, Bull. Am. Phys. Soc. **46**, 114 (2001).
[14] Z. Lin and W. W. Lee, Phys. Rev. E **52**, 5646 (1995).
[15] J. C. Strikwerda, *Finite Difference Schemes and Partial Differential Equations* (Chapman and Hall, New York, 1989), p. 298.
[16] Y. Nishimura, Z. Lin, J. L. V. Lewandowski, and S. Ethier, J. Comput. Phys. **214**, 657 (2006).
[17] Y. Nishimura and Z. Lin, Contrib. Plasma Phys. **46**, 551 (2006).
[18] A. Hasegawa and L. Chen, Phys. Rev. Lett. **35**, 370 (1975).
[19] A. Hasegawa and L. Chen, Phys. Fluids **19**, 1924 (1976).
[20] S. E. Parker and W. W. Lee, Phys. Fluids B **5**, 77 (1993).
[21] T. S. Hahm, W. W. Lee, and A. Brizard, Phys. Fluids **31**, 1940 (1988).
[22] A. Brizard, Phys. Fluids B **4**, 1213 (1992).

[23]P. H. Rutherford and E. A. Frieman, Phys. Fluids **11**, 569 (1968).
[24]S. E. Parker, Y. Chen, and C. C. Kim, Comput. Phys. Commun. **127**, 59 (2000).
[25]Y. Chen and S. Parker, Phys. Plasmas **8**, 441 (2001).
[26]F. L. Hinton and M. N. Rosenbluth (private communication); F. L. Hinton, M. N. Rosenbluth, and R. E. Waltz, Phys. Plasmas **10**, 168 (2003).
[27]R. B. White and M. S. Chance, Phys. Fluids **27**, 2455 (1984).
[28]H. Qu, Z. Lin, and L. Chen, "Gyrokinetic theory and simulation of mirror instability," Phys. Plasmas (in press).
[29]D. Biskamp, *Nonlinear Magnetohydrodynamics* (Cambridge University Press, Cambridge, 1993), p. 51.
[30]J. P. Goedbloed and S. Poedts, *Principles of Magnetohydrodynamics* (Cambridge University Press, Cambridge, 2004), p. 71.
[31]J. P. Goedbloed and H. J. L. Hagebeuk, Phys. Fluids **15**, 1090 (1972).
[32]J. Tataronis and W. Grossmann, Z. Phys. **261**, 203 (1973).
[33]W. Grossmann and J. Tataronis, Z. Phys. **261**, 217 (1973).
[34]C. M. Greenfield, J. C. DeBoo, T. H. Osborne, F. W. Perkins, M. N. Rosenbluth, and D. Boucher, Nucl. Fusion **37**, 1215 (1997).
[35]B. Scott, Phys. Plasmas **5**, 2334 (1998).
[36]Z. Lin, S. Ethier, T. S. Hahm, and W. M. Tang, Phys. Rev. Lett. **88**, 195004 (2002).
[37]E. M. Barston, Ann. Phys. (N.Y.) **29**, 282 (1964).
[38]C. Uberoi, Phys. Fluids **9**, 1673 (1972).
[39]G. Y. Fu and J. W. Van Dam, Phys. Fluids B **1**, 1949 (1989).
[40]B. D. Fried and S. D. Conte, *The Plasma Dispersion Function* (Academic Press, New York, 1961), p. 1.
[41]B. Coppi, M. N. Rosenbluth, and R. Z. Sagdeev, Phys. Fluids **10**, 582 (1967).
[42]G. Rewoldt, W. M. Tang, and R. J. Hastie, Phys. Fluids **30**, 807 (1987).
[43]J. Y. Kim, and W. Horton, Phys. Fluids B **5**, 4030 (1993).
[44]Y. Nishimura, Z. Lin, L. Chen, W. Wang, T. Hahm, and W. Lee, Bull. Am. Phys. Soc. **51**, 278 (2006).